SANDIA REPORT

SAND2016-9532
Unlimited Release
Printed September 2016

Metamaterial Receivers for High Efficiency Concentrated Solar Energy Conversion

Julius E. Yellowhair, Hoyeong Kwon, Andrea Alù, Robert L. Jarecki, Subhash L. Shinde

Prepared by
Sandia National Laboratories
Albuquerque, New Mexico 87185 and Livermore, California 94550

Sandia National Laboratories is a multi-mission laboratory managed and operated by Sandia Corporation, a wholly owned subsidiary of Lockheed Martin Corporation, for the U.S. Department of Energy's National Nuclear Security Administration under contract DE-AC04-94AL85000.

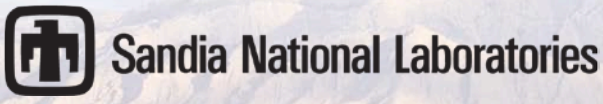

Issued by Sandia National Laboratories, operated for the United States Department of Energy by Sandia Corporation.

Available to DOE and DOE contractors from
U.S. Department of Energy
Office of Scientific and Technical Information
P.O. Box 62
Oak Ridge, TN 37831

Telephone: (865) 576-8401
Facsimile: (865) 576-5728
E-Mail: reports@osti.gov
Online ordering: http://www.osti.gov/scitech

Available to the public from
U.S. Department of Commerce
National Technical Information Service
5301 Shawnee Rd
Alexandria, VA 22312

Telephone: (800) 553-6847
Facsimile: (703) 605-6900
E-Mail: orders@ntis.gov
Online order: http://www.ntis.gov/search

SAND2016-9532
Unlimited Release
Printed September 2016

Metamaterial Receivers for High Efficiency Concentrated Solar Energy Conversion

Julius E. Yellowhair[1], Hoyeong Kwon[2], Andrea Alù[2], Robert L. Jarecki[1], Subhash L. Shinde[1]

[1]Concentrating Solar Technologies Department
Sandia National Laboratories
P.O. Box 5800
Albuquerque, New Mexico 87185-MS1127
(505) 844-3029, jeyello@sandia.gov

[2]University of Texas at Austin
Department of Electrical and Computer Engineering
Austin, TX 78701

Abstract

Operation of concentrated solar power receivers at higher temperatures (>700°C) would enable supercritical carbon dioxide (sCO_2) power cycles for improved power cycle efficiencies (>50%) and cost-effective solar thermal power. Unfortunately, radiative losses at higher temperatures in conventional receivers can negatively impact the system efficiency gains. One approach to improve receiver thermal efficiency is to utilize selective coatings that enhance absorption across the visible solar spectrum while minimizing emission in the infrared to reduce radiative losses. Existing coatings, however, tend to degrade rapidly at elevated temperatures. In this report, we report on the initial designs and fabrication of spectrally selective metamaterial-based absorbers for high-temperature, high-thermal flux environments important for solarized sCO_2 power cycles. Metamaterials are structured media whose optical properties are determined by sub-wavelength structural features instead of bulk material properties, providing unique solutions by decoupling the optical absorption spectrum from thermal stability requirements. The key enabling innovative concept proposed is the use of structured surfaces with spectral responses that can be tailored to optimize the absorption and retention of solar energy for a given temperature range. In this initial study through the Academic Alliance partnership with University of Texas at Austin, we use Tungsten for its stability in expected harsh environments, compatibility with microfabrication techniques, and required optical performance. Our goal is to tailor the optical properties for high (near unity) absorptivity across the majority of the solar spectrum and over a broad range of incidence angles, and at the same time achieve negligible absorptivity in the near infrared to optimize the energy absorbed and retained. To this goal, we apply the recently developed concept of plasmonic Brewster angle to suitably designed nanostructured Tungsten surfaces. We predict that this will improve the receiver thermal efficiencies by at least 10% over current solar receivers.

ACKNOWLEDGMENTS

Sandia National Laboratories is a multi-mission laboratory managed and operated by Sandia Corporation, a wholly owned subsidiary of Lockheed Martin Corporation, for the U.S. Department of Energy's National Nuclear Security Administration under contract DE-AC04-94AL85000.

CONTENTS

FIGURES

NOMENCLATURE

AMAT	Applied Materials and Technologies
ASML	Advanced Semiconductor Materials International (Dutch company)
BARC	Base Anti-Reflective Coating
CMP	Chemical Mechanical Polish
CSP	Concentrating Solar Power
CVD	Chemical Vapor Deposition
DOE	Department of Energy
E-BEAM	Electron Beam
GPa	Giga Pascals
GW	Giga Watts
HSUSG	High Stress Undoped Silicate Glass
IR	Infrared
MDL	Microelectronics Development Laboratory, also known as “SiFab”, the Silicon Fab segment of MESA
MESA	Microsystems and Engineering Sciences Applications
NA	Numerical Aperture
O&M	Operations and Maintenance
PETEOS	Plasma Enhanced Tetra Orto Silicate
PR	Photoresist
PVD	Physical Vapor Deposition
SNL	Sandia National Laboratories
Si	Silicon
TiN	Titanium Nitride
UV	Ultra Violet (radiation)
W	Tungsten Symbol

1. INTRODUCTION

Concentrating Solar Power (CSP) uses thermal energy collected from sunlight to produce utility-scale electricity. Currently there is approximately 1.6 GW deployed CSP plants in the U.S. and 4.4 GW worldwide [1]. The Department of Energy (DOE) SunShot initiative started in 2011 placed aggressive techno-economic targets on solar technologies including CSP systems to reach grid parity (with fossil fuel electricity) by 2020 [2]. To meet SunShot goals, costs must be reduced and/or performance increased on all subsystems of a CSP plant. To increase the performance of a CSP receiver, the thermal energy from sunlight must be efficiently collected and retained, which in turn could reduce the collector field size and further reduce the installation cost. The current standard for CSP receiver coatings is the high-temperature Pyromark 2500, a black paint with high solar absorptance (>95%), but also high thermal emittance (~87%) at elevated temperatures. Pyromark is known to degrade when exposed to high temperatures, necessitating reapplication (typically every 5years) to the receiver surface, which adds to the O&M cost. Another solution to improve thermal efficiency is to utilize selective coatings that enhance absorption across the visible solar spectrum while minimizing emission in the infrared regime to reduce radiative losses. Previous work at Sandia to find alternatives to Pyromark has emphasized the development of new materials that intrinsically possess the proper optical properties and mechanical stability. Success in achieving the desired optical properties has been shown for metal oxide spinels, in particular cobalt-based spinels, but the mechanical stability of the materials at high temperatures and high solar flux has been poor [4-6]. Thus, currently selective coatings tend to degrade at high temperatures.

Recently, there has been interest in incorporating super-critical CO_2 (sCO_2) power cycles, which require higher inlet temperatures around 700°C. The higher temperature also improves the thermo-dynamic power cycle efficiencies, anticipated to be $\geq$50% for sCO_2. With current receiver coatings, the thermal efficiency of the receiver goes down due to the radiative and convective losses. The radiative losses in particular increases dramatically with increasing temperature. To address this issue, we propose metamaterial structures on the receiver surfaces that will efficiently absorb and retain incident solar energy. Metamaterials are a promising solution to the performance and reliability challenges for high-temperature solar energy harvesting.

Previous work in metamaterials has shown the ability to achieve sub-diffraction limit imaging, sub-wavelength volume light sources, negative indices of refraction, and several others exotic properties [7-8]. Engineering the absorption/emission spectra of surfaces using metamaterials has found applications in thermal photovoltaics, environmental sensing, and security and defense. Metamaterials have also been investigated as a means to improve the efficiency of photovoltaics. Some recent theoretical and experimental work has been applying the same concepts to create spectrally-selective surfaces in the visible and near-IR that more effectively absorb and retain solar radiation as thermal energy [9-11]. However, demonstrations of such absorbers have primarily been performed only at room temperature, with just a handful considering performance at flux and temperature levels typical of current CSP applications [9]. Therefore, the engineering of high-temperature metamaterials for CSP is a new field of research. Spectrally-selective metamaterial absorbers have the potential to be a paradigm shifting technology that creates a fundamentally new approach to the optimization of CSP receiver surface design. Although not part of the work reported here, lessons learned about metamaterial design and operation can also be applied to a

number of research areas at Sandia, such as cloaking, camouflage, antenna-design, and other energy-on-demand concepts.

This project focused on exploring theoretical, numerical and some experimental efforts: the prospect of finding suitably designed infrared/optical metamaterials based on different refractory materials to significantly improve high-temperature (>700°C) CSP receivers. Spectrally-selective surfaces, in the CSP context, are characterized by high absorptance at wavelengths below some cut-off wavelength and low absorptance above that cut-off wavelength. At higher temperatures, the peak wavelength of the blackbody thermal radiation shifts to shorter wavelengths (Wien's displacement law) and the overlap between the solar spectrum and blackbody spectrum becomes more significant as shown in Figure 1. For a given temperature, flux concentration and absorption spectrum, there exists a cut-off wavelength that optimizes the net irradiance absorbed and retained.

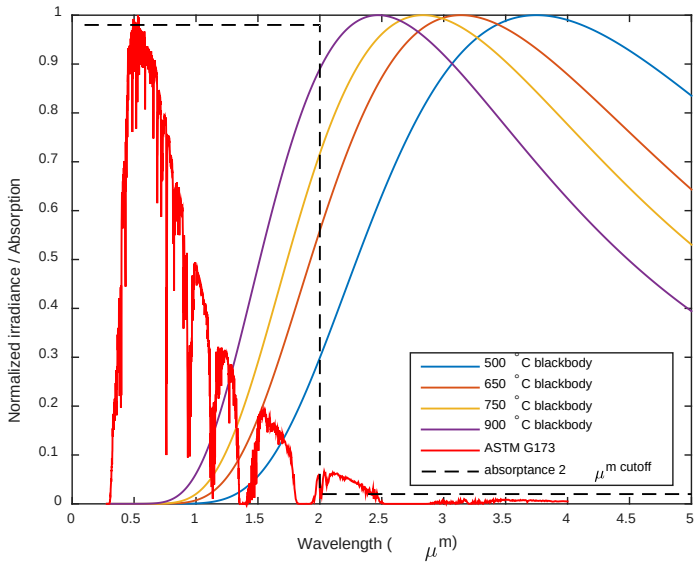

Figure 1. Comparison of terrestrial solar spectrum (red), blackbody spectra for various receiver temperatures, and absorptance spectrum for an idealized selective absorber. All the curves are normalized.

Metamaterials are periodic structured media whose optical properties are determined by sub-wavelength structure features instead of the bulk material properties, providing a unique solution to this challenge by decoupling the optical and thermal stability requirements. The key enabling innovative concept proposed is the use of custom designed surface structures with spectral responses that can be tailored to optimize the absorption and retention of solar energy for a given operating temperature. The customized spectral response of the metamaterial surface is dictated by the engineered interaction between the incident photons and highly localized surface waves at metal-dielectric interfaces (surface plasmons), enabled by surface structuring and patterning. The goals are to tailor the optical properties for high (near unity) absorptivity across the majority of the solar spectrum and negligible absorptivity in the near infrared in order to optimize the energy absorbed and retained. Since the optical properties, specifically the absorptance and emittance, of the metamaterial are determined by the spacing and feature sizes of the metamaterial architecture, once a suitable base material is identified, a metamaterial enhanced absorber can be tailored to a wide range of applications and operating temperatures. Our future plan is to also identify optimum

metamaterial substrates based on their stability in the expected harsh environment and their compatibility with microfabrication techniques and optical performance.

There has been many applications and significant material development for solar receiving structures, manipulating the material properties and the interaction between materials to achieve high absorption efficiency. Instead of focusing on the properties of the solar cell material, designing structures that can largely enhance light absorption regardless of materials is an interesting venue in the context of nanophotonic engineering. To achieve high absorption in a certain structure, extraordinary transmission (EOT) and multiple resonant techniques have been used and explored so far. However, they have the serious drawback of narrow bandwidth, which is not compatible with the typical broad bandwidth of available solar spectrum. To overcome this restriction, it has been proposed in recent papers that broadband absorption may be achieved using impedance matching at the Brewster angle for an array of narrow slits [11]. At the so-called plasmonic Brewster angle [12] perfect transmission and large energy concentration in the slits, essentially independent of the incidence frequency, can be achieved. Interestingly, this phenomenon can be translated directly to enhance energy absorption, as explored in this research project, and extended to broad angular beamwidth, weak polarization dependence, and spectrum selectivity to enhance energy efficiency.

First, we explored the design aspects of *ultrabroadband absorbers* with large angular collection range based on patterned refractory metals, using the concept of plasmonic Brewster angle recently introduced in our group [12]. We explored patterned metallic surfaces that can absorb significant portions of the near-infrared and visible spectrum over a broad angular spectrum made possible by the unusual impedance matching scheme achieved by properly carving slits in a refractory metallic screen. This will enable us to tailor to a large degree the absorption spectrum of thin metasurfaces in the range of wavelength of interest, specifically the terrestrial solar spectrum.

As a second interesting direction of exploration in the same context of broadband absorbers, we explored the use of non-resonant metasurfaces able to trap light and enhance absorption over a very broad range of wavelengths by properly designing transverse inhomogeneities. As we have recently shown theoretically and numerically (N. Mohammadi Estakhri, et al.), engineering specifically tailored transverse gradients of the reflection phase in a patterned metasurface allows us to trap light and increase the absorption path over a very broad range of frequencies, an ideal response to realize broadband absorbers.

Finally, we combined these approaches to broadband absorption with the exploration of dispersion engineering of refractory metamaterials to *suppress thermal emission* at wavelengths longer than 2 μm, targeted for the range of devices typically used in high-temperature solar thermal energy-harvesting applications. This will allow significant boosting of the overall efficiency of current solar absorber systems. This will be achieved by combining the previous concepts with proper band engineering of optimized metamaterials, achieved with photonic crystal and metamaterial concepts.

Combining these three techniques, and tailoring them for refractory materials, will result in overcoming several known limitations of conventional high-temperature energy harvesting systems, paving the way to exciting novel concepts for concentrating solar thermal, thermo-

photovoltaic, photovoltaic and green-energy applications. This work has the potential to have groundbreaking impact on the physical understanding and on the application of nanoscale materials and metamaterials with refractory properties, and will open several new scenarios for energy devices and systems.

The overarching technical goals for this work are to (1) develop metamaterial architecture designs for a selective absorber with high absoprtance (>0.95) in the solar spectrum and low thermal emittance (<0.1) in the infrared spectrum which will optimize the absorption and retention of solar energy, (2) identify base material for the metamaterial architecture that is compatible with microfabrication and thermally stable at 700°C, (3) fabricate metamaterial samples that will be characterized to demonstrate enhanced optical performance and thermal stability. For the study reported here Tungsten was chosen as the initial material to evaluate. The initial fabrication recipe was developed, which will be refined and optimized in future projects.

2. METAMATERIAL DESIGN AND SIMULATIONS

Concentrated solar power systems rely on solar absorbers on the receiver to efficiently convert incident solar radiation to thermal energy and then to electric power. A power cycle that uses sCO_2 as the working fluid is especially of interest due to expected high efficiencies (>50% thermal to electric) at elevated temperatures (~700°C) and its small physical footprint. To integrate a sCO_2 power cycle with a concentrated solar collector and receiver system, more efficient selective receiver surfaces are needed that have both high solar absorptance and low thermal emittance in the near infrared (NIR) portion of the blackbody thermal radiation. Additionally, the surfaces must be mechanically stable in air to avoid repeated and costly replacement of the surfaces. At present, the best candidate materials are high temperature refractory metals, such as Tungsten, and Silicon Carbide (SiC), which is stable at high temperatures and harsh environments.

In this section, we discuss the development of the metamaterial design for high absorptivity in the visible spectrum and low absorptivity (or high reflectivity) in the near IR region, which suppresses thermal re-radiation. Tungsten and silicon (Si) were the initial materials simulated: Tungsten is a high temperature refractory metal, and silicon is a semiconductor for which microelectronic processing is developed and very mature.

2.1. Theoretical Basis

In classical optics, when light is incident on an interface of two dielectric media (e.g., free space and glass), some of the light is reflected while the rest is transmitted into the media on the refraction side. At some incidence angle, all the light will be transmitted into the second media. This incidence angle is called the Brewster angle. It is achieved when the impedance of the two media are matched. The ideal property of Brewster's angle is it is inherently broadband. Metals on the other hand have an impedance of zero so the incident light is completely reflected off metal surface. However, if slits are cut into a thin metal sheet where the impedance over the slits are non-zero, the average impedance of the metal sheet with slits can be non-zero as well. The slit width can be varied to impedance match to the dielectric material on the light incidence side.

Ideal transmission in a periodic slit structure can achieved by matching the impedance from free space and unit cell of the structure based on the plasmonic Brewster angle concept described by Argyropoulos [11]. The idea is that, as the wave hits an array of slits in an opaque material (Figure 2), at normal incidence the impedance mismatch is very large. However, the structure may be designed such that for transverse-magnetic (TM) incidence the wave impedance matches the average impedance of the slit array, allowing ideal energy squeezing into the slits. This effect is weakly dependent on frequency and polarization, and the Brewster angle can be found as:

$$\theta_B = \cos^{-1}\frac{\beta_s w}{\varepsilon_s k_0 d}, \tag{1}$$

where ε_s is the permittivity of the filling material in the slits, considered as free space in this report, β_s is the guided vector in the slits and the parameters, *w* and *d*, are given in Figure 2. When a TM mode is excited in the slit, a plasmonic mode propagates along the metallic surface with β_s as the wave propagation constant, satisfying the transcendental equation [13]

$$\tanh[\sqrt{\beta_s^2 - k_0^2}\,\frac{w}{2}]\sqrt{\beta_s^2 - k_0^2} = \frac{-\sqrt{\beta_s^2 - k_0^2\varepsilon_m}}{\varepsilon_m}. \tag{2}$$

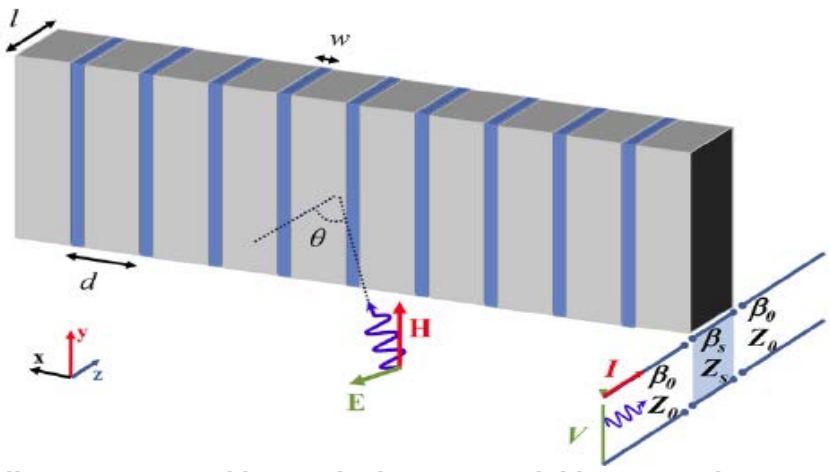

Figure 2. Periodic structure and its equivalent TL model in TM mode propagation [11].

From Equation 2, it can be seen that a guided vector is not related to incidence angle but only to the permittivity of material and slit width, *w*. This shows that the impedance of the unit cell structure (shown in Figure 3a) is independent of the incident angle. When the slit width, *w*, and the structure's material is set, the guided vector can be derived with the relationship above. Normally, the real part is much larger than the imaginary part, which determines the amount of dissipation as the wave propagates in the slit. High absorption is also related to the structure's length. To increase the absorption efficiency in a limited length, we can use tapered slits. The wave squeezed into the slit will be guided by tapered structure. Slow varying taper offer an adiabatic process, which makes the efficiency higher than those with no taper structure.

2.2. Design and Application

Based on the previous theory, a solar cell structure, for example, can be designed and optimized to support the desired Brewster angle independent of the incidence plane using the unit cell sketched in Figure 3. The bottom layer of the tapered structure is also composed of the same material as the slit walls. Since for our application we care about broad beamwidth and weak dependence on polarization, we design the structure to absorb at a Brewster angle very close to normal incidence, so that the absorption window spans over a broad angular range, and it is weakly affected by polarization in the range around the normal incidence. The performance of Tungsten (W) and silicon (Si) were investigated through simulations. Permittivity of Tungsten is derived from the 'Handbook of Optical Constants of Solids' [17]. Si, including highly doped Si, properties were provided by the Sandia National Laboratories.

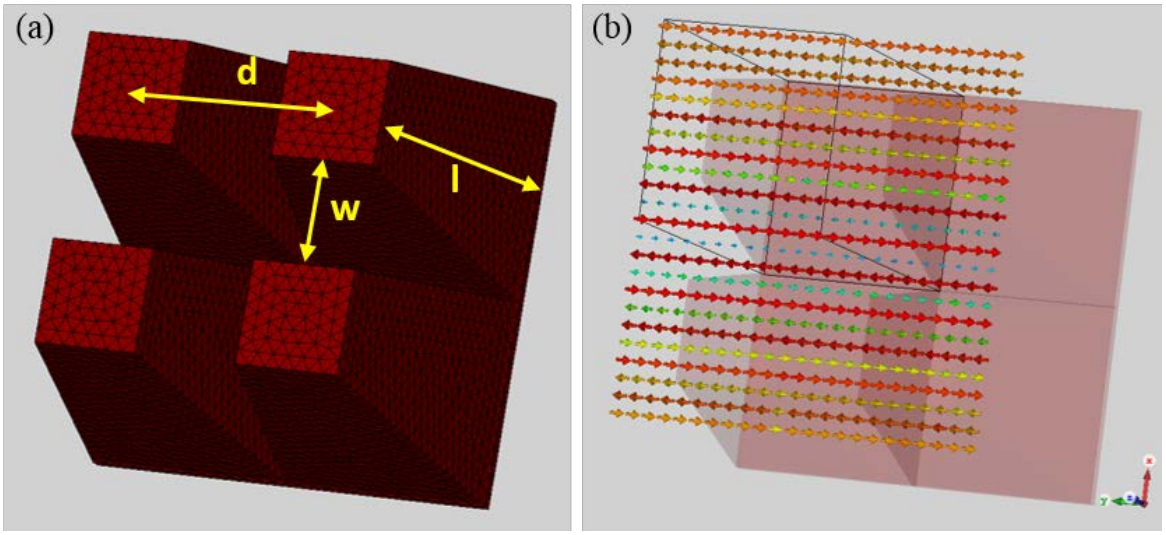

Figure 3. (a) CST [16] model of a unit cell of the structure; material can be Tungsten. *d* is the periodicity, *w* is the slit width, *l* is the taper length. (b) H-field distribution for a TM polarized wave incident on the structure.

2.3. Results and Discussion

To evaluate the effects of each design variable on the absorption window, we analyzed the effect of changing the ratio between slit width, *w*, and periodicity, *d*, and the length of the structure, *l*. The goal of this analysis was threefold: first, we controlled the angular range of absorption, showing that one can achieve omnidirectional absorption and directive absorption using refractory materials; second, we controlled the frequency range over which high absorption is available, and understand how the design parameters can modify this range, given that the Brewster phenomenon is in principle frequency independent; and finally, we explored the relationship between materials employed and absorption.

2.3.1. Adjusting Brewster angle in absorption

The plasmonic Brewster angle is governed by Equations 1-2, which is typically controlled by the wavenumber in the slits. Figure 4 shows, as an example, the calculated guided vector normalized

to the wavenumber in free-space for a slit width, w = 200nm. The figure indicates that the ratio β_s / k_0 is flat over a very broad frequency range, since the guided mode is very close to the light line, as long as the slit width is larger than 100 nm. In this regime of interest for our project, the Brewster angle is essentially frequency independent, and governed only by the geometrical parameter w/d:

$$\theta_B = \cos^{-1}(w/d) \tag{3}$$

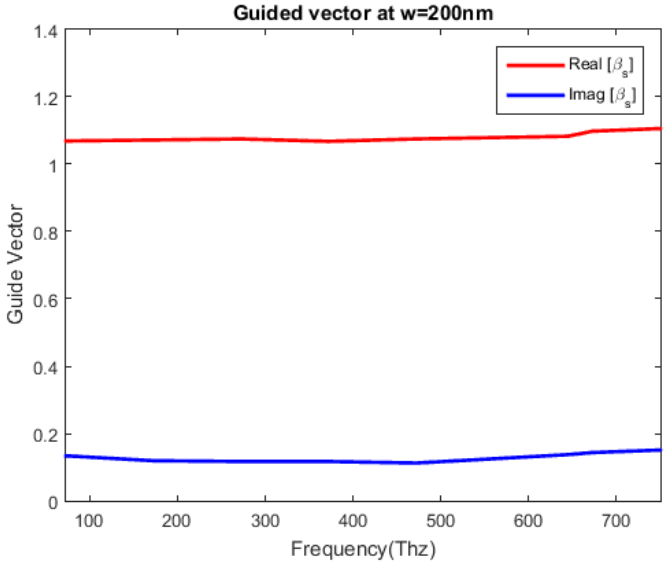

Figure 4. Real and imaginary parts of the guided vector for Tungsten (W) with w = 200 nm that cover the visible spectrum and IR.

When the ratio w/d is not too small, the Brewster angle gets closer to 0° and high absorption can occur over a broad, almost omnidirectional range in angle, θ. On the other hand, when w/d is close to zero, the Brewster angle gets close to 90°, and it drastically narrows down, which may have interesting applications for selective absorbers or emitters. This can be clearly seen by calculating the reflection coefficient and measuring the amount of transmitted light at the surface of the structure. The impedance of TM waves in free-space, Z_0, and the surface impedance of the structure, Z_s, are respectively

$$\begin{aligned} Z_0 &= \eta_0 d \cos\theta_i \\ Z_s &= w\beta_s / c\varepsilon_0 \end{aligned} \tag{4}$$

Then the reflection coefficient, R, and transmission coefficient, T, are evaluated as,

$$R = \frac{Z_s - Z_0}{Z_s + Z_0}, \quad |T|^2 = 1 - |R|^2 \tag{5}$$

From these relationships, we find an analytical interpretation of absorption in terms of incident angle θ_i. To compare the extreme two cases, we explore the cases for which the ratio *w*/*d* is 0.1 and 0.5 in a structure made of Tungsten. The Brewster angle is respectively about 84.3° and 60°. As discussed above, low Brewster angle structures offer omnidirectional absorption and high Brewster angle structures give specific directionality in absorption as shown in Figure 5.

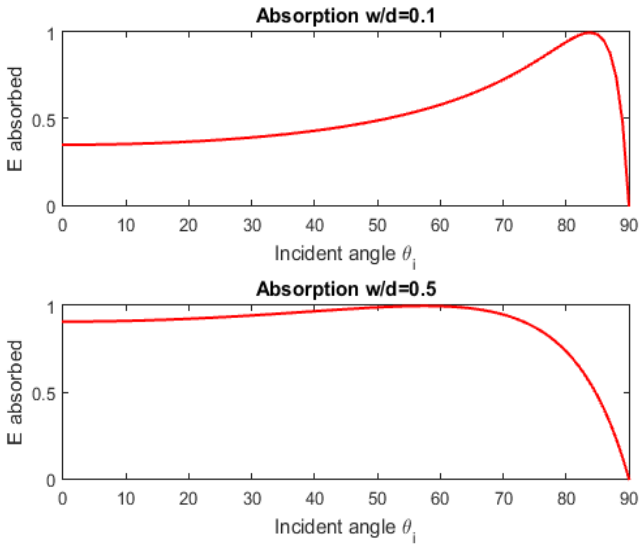

Figure 5. Absorption measured at frequency = 400 THz varying θ and *w*/*d*. Brewster angle in (a) is around 85°, in (b) it is 60°.

The two structures provide different functionalities: in the first scenario, with omnidirectional absorption, a large amount of light energy can be harvested into the structure, which when combined with the inherent broad bandwidth of the phenomenon, makes it ideal for the purpose of this project. The incident angle does not have significant effect on absorption. But if the Brewster angle is close to 90°, the absorption is high only near the Brewster angle, providing directive absorption / emission.

In Figure 6 we explored the dependence of these absorption spectra as a function of both angle and frequency. In this figure, it is evident how the described absorption properties are preserved with frequency, realizing a quite interesting absorption/emission profile for various applications. In Figure 6a the slit width, *w*, is 6 nm, and the real part of β_s / k_0 is around 2. From calculations, the Brewster angle θ_B = 60° in (a) and 80° in (b), which is confirmed by the full-wave simulations in the figure. Observing the directivity of absorption, in Figure 6a, omnidirectional absorption can be achieved over broad bandwidths almost above 80% in a large range of incident angles. But in Figure 6b, the absorption is only high near the perfect transmission window at $\theta_B = 80^\circ$. Following the previous discussion, absorption in the structure for which the slit width, *w*, is larger than 100 nm provides an amount of absorption that is almost independent of the slit width. To highlight this property, simulations were performed for two cases: one with *w* = 250 nm, *d* = 500 nm and another with *w* = 300 nm, *d* = 600 nm. The length of the structure is fixed at 1000 nm. The result is shown in Figure 6c-d. Brewster angles in both structures are around 60° with different slit width

and periodicity. Due to impedance matching between the surface of the structure and free space, each slit width and periodicity has no effect on the amount of energy harvested. Light is squeezed into each slit and shows high absorption regardless of the structure size.

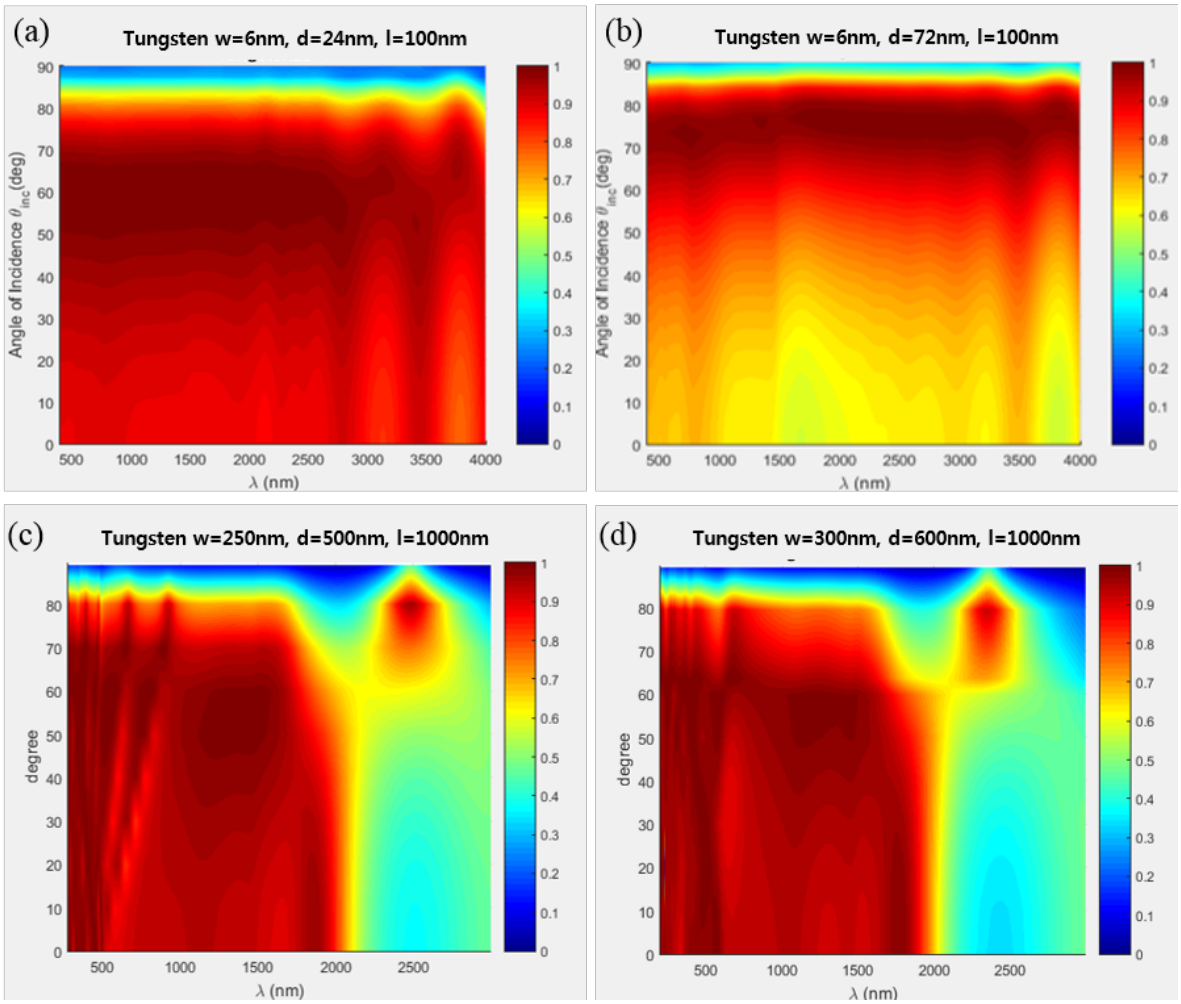

Figure 6. All four structures are made of Tungsten and show the absorption angular and frequency spectra for: (a) slit width *w* = 6 nm, periodicity *d* = 24 nm, (b) *w* = 6 nm, *d* = 72 nm. Omnidirectional absorption and directional absorption can be compared with (a) and (b). (c) Slit width *w* = 250 nm, periodicity *d* = 500 nm, (d) *w* = 300 nm, *d* = 600 nm. Also omnidirectional absorption is observed in both structures.

2.3.2. Manipulating the frequency band of transmission

Omnidirectional absorption is related to the structure's transverse grating design, and can be achieved by applying the plasmonic Brewster angle concept on the surface of the structure. Another important challenge for this project is to be able to control the bandwidth of absorption. The difference of absorption over the frequency range depends on the imaginary part of the guided vector along the grating, as determined by the slit width in Equation 2. In this sense, one can use a couple of important metrics to ultimately control the bandwidth of absorption: first, by tapering the slit waveguide we are able to control β_s along the slit, and therefore slow down the wave and

absorb it over a shorter electrical distance. Of course, this absorption has an ultimate cut-off with frequency: the lower absorbed frequency has to comply with Rozanov's bound on the thickness of absorbers [18]. Therefore, the structure length, *l*, is expected to ultimately determine the lower cut-off for the frequency range of absorption. At the same time, the upper cut-off is ultimately determined by the transverse period, *d*, which controls the range of frequencies for which no higher-order diffraction is expected, and therefore for which our impedance model for the surface of our structure holds. We verify these considerations with full-wave simulations in the following figures.

The imaginary part of guided vector is much larger when $w = 6$ nm compared to $w = 250$ nm, with the effect of slowing down the wave in the taper and enhance absorption. This is why the absorption in Figure 6a has a cut-off frequency much lower than in Figure 6c, even though the length of the structure in (c) and (d) is ten times the one in (a) and (b). When the slit width is set, the absorption depends on the length of the total structure. After the wave is guided to the bottom plate, part of it will be reflected back and decay again along the taper structure. The bottom plate, which is thicker than skin depth, also contributes to a certain amount of absorption, although small. To show how the length of the structure affects the absorption, we simulated structures with same Brewster angle and different lengths made with Si. Comparing Figure 7a and Figure 7b, Brewster angle is 75.5° in both cases but the wavelength that gives high absorption stops around 600 nm for a length of structure equal to 1000 nm. In Figure 7b, instead, with a length of 3000 nm, the absorption is large in the same angular range and goes far beyond 800 nm. Similar considerations apply to the designs in Figure 7c-d, for which the Brewster angle is different. Here, as in the previous figures, the material properties also play a role, since Si is essentially transparent below its bandgap, affecting the overall absorption for longer wavelengths. It is seen indeed how the absorption does not change dramatically in this region even if the structure is three times as long. This issue is further discussed in the next section, as we deal with the material properties.

For these structures, the lower cut-off is clearly seen in the wavelength axis. This sharp cut-off line comes from Si's electrical properties. However, if the material is lossy like in the case of metals, the cut-off line is not as clear and provides a transition of absorption similar to Figure 8a (in which we consider Tungsten). Since in our case we are interested in a sharp transition between regions with high and low absorption, in these scenarios controlling the tapering can help sharpen the contrast. Figure 8, for instance, considers the case in which we remove the tapering in the slits, completely suppressing the absorption above the cut-off wavelength. Tapering allows part of the energy above cut-off to be absorbed. The upper right inset in Figure 8b shows the modeling of the non-tapered structure. In this case, both structures are made of Tungsten, which allows absorption throughout the infrared region.

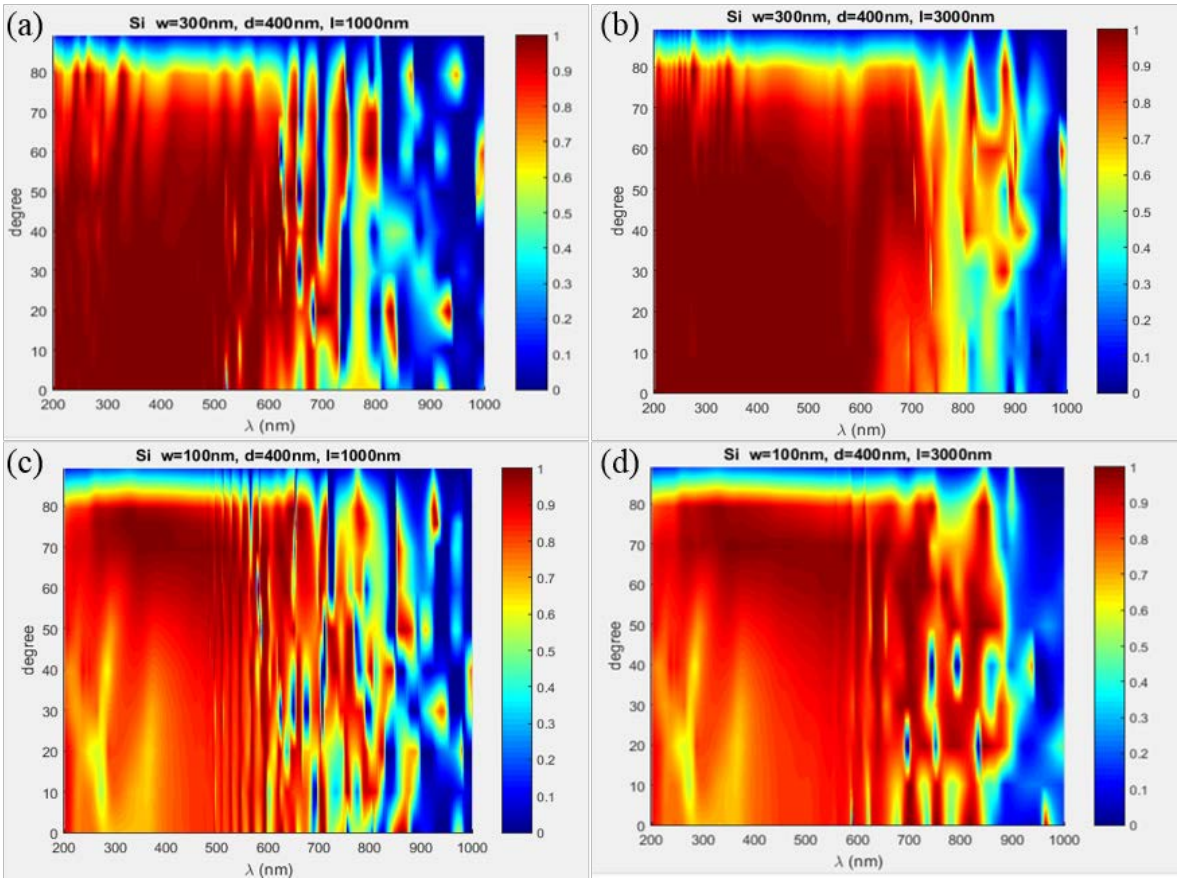

Figure 7. Structures are made of Si. (a)-(b) and (c)-(d) have the same Brewster angles, showing the effect of increase in length on the cut-off wavelength.

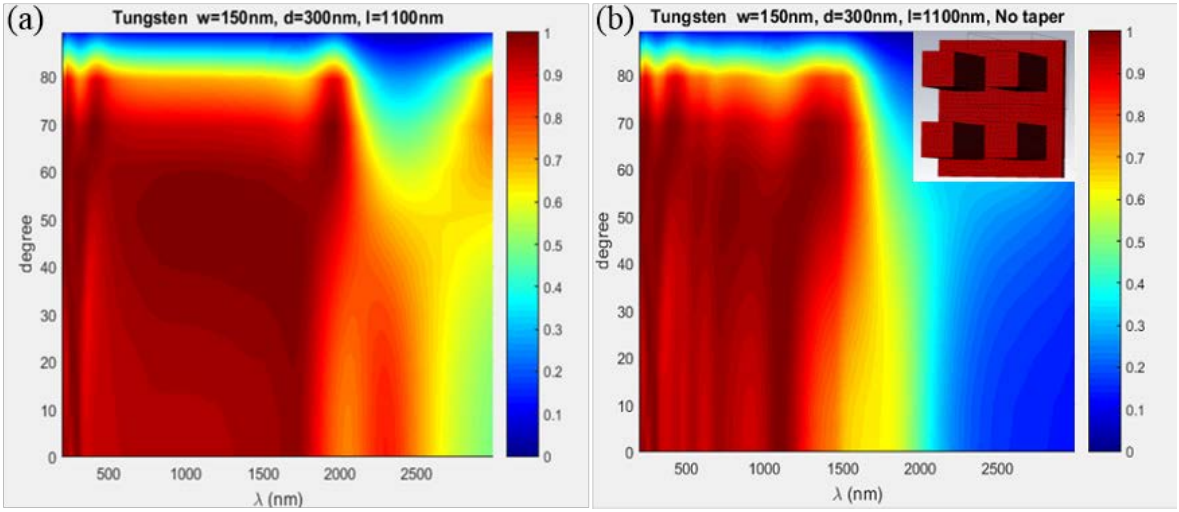

Figure 8. The structures are made of Tungsten (W), with same slit width and periodicity. The cut-off wavelength is around (a) 1500 nm and 2000 nm, as seen in the non-tapered structure (b). On the other hand, a transition beyond the cut-off wavelength arises in the tapered structure (a). The inset shows the geometry for the non-tapered case (i.e., vertical walls).

2.3.3. Material properties and absorption

The material properties are also closely related to the guided vector within the slit, as governed by Equation 2. When we discuss the propagation and absorption in arbitrary materials, it is intuitive to expect that lossy materials support a large amount of absorption, which implies a large imaginary part of the guided vector. In this project, we have analyzed different material properties, focusing on Tungsten and silicon, which appear the most appealing in terms of fabrication. Tungsten (W) is a metal and has a large value of negative real part of permittivity in the frequency range of interest. In Figure 9a, the permittivity increases both in the real and imaginary parts beyond 4000 nm in wavelength. Highly doped silicon (P-plus Si) and undoped silicon (Si) are semiconductors. Highly doped silicon has an energy band close to the conduction band due to high density of electron donors, and acts like a conductor given free mobility of electrons. This is observed in Figure 9b, showing that the imaginary part of permittivity is larger than Tungsten permittivity. On the other hand, undoped Si is absorptive in the visible, but transparent in the infrared range.

In order to explore the effect of permittivity dispersion on broadband absorption, each structure in Figure 9 is designed with the same length l = 1000 nm and same design parameters. Comparing the permittivity dispersion in Figures 8a-b, the imaginary part of P-plus Si is much larger than the one of Tungsten, which instead has a larger negative real permittivity. For the same length, P-plus Si structures show broader bandwidths than Tungsten, whose absorptivity is cut off around a wavelength of 2000 nm. Even though Si has a smaller value of permittivity, it can achieve high absorption in certain range of wavelengths when applying the Brewster angle concept during the designing of the structure. However, due to its material bandgap, getting high absorption beyond 600 nm is difficult for the same length of 1000 nm, compared to other materials. As discussed in previous section, increasing the length of the structure does not have a significant effect in this case, because the imaginary part of permittivity itself converges to zero above around 500 nm wavelength.

Employing P-plus Si, as shown in Figure 9d, can provide ultra-broadband absorption over wavelengths that go over 4000 nm for a structure with just 1 μm thickness. Overall, it appears that Tungsten fits better with the overall purpose of this program, since it can withstand high temperatures, it can tune the frequency range of high absorption, and provides very large flexibility in design throughout the optical and infrared frequency range. P-plus Si and Si are restrictive, due to their low fusion temperature and permittivity dispersion.

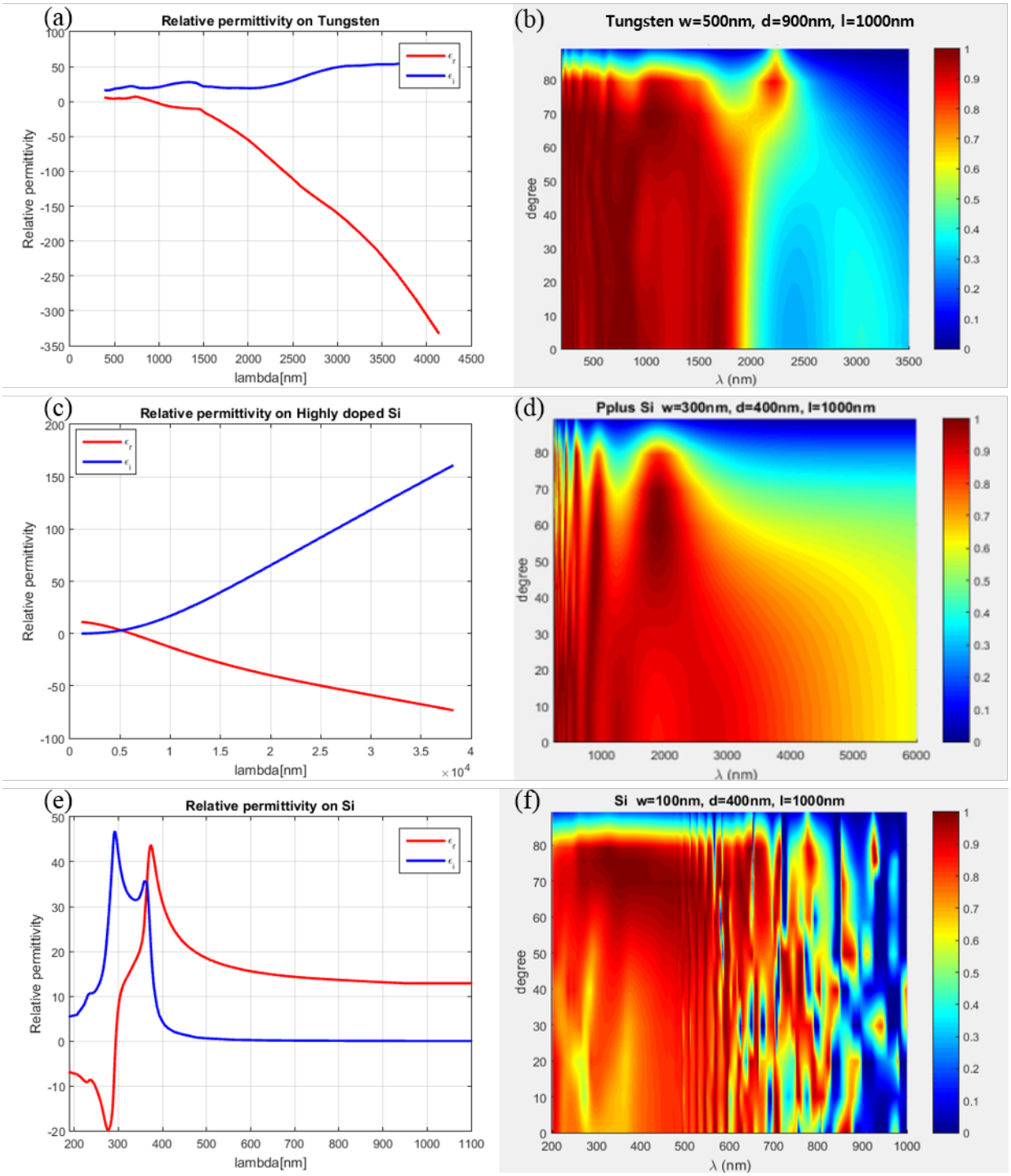

Figure 9. (a) Permittivities of (a) Tungsten, (c) highly doped silicon, and (e) silicon. (b), (d), and (e) show the corresponding absorption spectra. The geometry in (b) is *w* = 500 nm, *d* = 900 nm (Tungsten), (d) is *w* = 300 nm, *d* = 400 nm (P-plus silicon), and (e) is *w* = 100 nm, *d* = 400 nm (silicon).

3. METAMATERIAL STRUCTURES FABRICATION APPROACH

One of the technical challenges of this project is identifying materials that are stable at high temperatures, inclusive of the necessary plasmonic properties, and compatible with mass microfabrication processes. Operation conditions, and optical properties favor refractory metals as the primary structured solar absorber construction material. Since relatively thick, high aspect ratio structures are also required, chemical vapor deposition (CVD) of Tungsten from the SiFab within MESA in Bldg. 858N (at Sandia) seemed to be the obvious first choice for initial experiments. The AMAT W-CVD Centura tool offers standard $WF_6/SiH_4/H_2$-based deposition recipes of up to 1200 nm in thickness, sufficient for interesting devices such as those proposed in this work.

Tungsten (W) has the helpful property that dry plasma etches using fluorine-based chemistries exist, although typically used for much thinner W films of perhaps 100 nm in thickness. PVD (physical vapor deposition, in this case by reactive sputtering of titanium in N_2 ambient) titanium nitride (TiN) is an available good adhesion and barrier layer for W-CVD deposition on Si or SiO_2, and TiN also is a refractory material with excellent thermodynamic stability. Complications with the use of W-CVD include a very high tensile stress of around 1.3 GPa which tends to produce excessive wafer bow, a grainy structure and rough film surface, low etch selectivity with photoresist masks, and the lack of demonstrated successful high-aspect ratio etching processes.

For the ultimate levels of nanostructuring needed, e-beam lithography is an interesting option, but since deep-UV optical lithography is much faster, and thus can generate much larger testable absorber device areas on a wafer, and since sub-200 nm features approaching 150 nm are feasible, the deep-UV optical lithography approach was down-selected for the initial work. The other fabrication elements have been chosen to allow extension to e-beam lithography in future.

Figure 10 shows the process plan utilized for the initial SiFab lots. Twenty-four standard MDL part #2015, 150 mm diameter P-type Si monitors were used as wafer substrates. After lot start and scribe, a thick 5 μm layer of front side HSUSG was deposited as a compressive stress compensator. In metals, 25 nm of TiN was deposited as an adhesion layer, and then 1.2 microns of CVD Tungsten was deposited on top of that at 475°C. A laser scanning wafer curvature measurement was conducted to confirm good stress compensation and wafer flatness. Wafers were sent to the chemical mechanical polishing (CMP) area where a short touch polish process was developed to reduce surface roughness, which may have otherwise interfered with later lithography and etch steps, with only about a 75 nm loss in Tungsten thickness, as confirmed by automated 4-point probe resistivity measurements, and additional wafer curvature measurements. The wafers then traveled to the CVD area, where an Applied Materials P-5000 dielectric deposition tool was used to add 500 nm of PETEOS, followed by 200 nm of plasma-enhanced amorphous-Si to serve as a hard mask. The idea is to allow the 500 nm PETEOS to serve as the primary final W-etch mask with greater durability than the original thinner and more fragile UV210 photoresist. The function of the a-Si layer in turn is to provide sufficient mask to etch openings in the 500 nm PETEOS, after a Si dry etch is used to transfer the original PR mask pattern to that a-Si layer. See Figure 11.

SubPlan	Step	Step Description	Tool/Location	Step Seq	COMMENT
StartLot	LOT0000	allocate wafers	zLOTArea	'0000	
	LOT0001	Start lot	zLOTArea	'0001	
	LOT0002	EDC for more wafers	zLOTArea	'0002	
	LOT9150	check wafer type	zLOTArea	'0003	
LUMScribe	LOT9250	bare silicon scribe	LUM1	'0004	
	LOT1220	SC-1 megasonic clean	WB17-TANK2	'0005	
	LOT0918	spin rinse dry	SRD17or18or19or20	'0006	
HS_USG_STACK	CVD2999	special	PSKA-TEOSorPSKB-PSGPENorPSKC-SPUTR	'0007	5 um total = 2um+2um+1um of HSUSG frontside deposition, to serve as significant pre-compensation for tensile 1.2 um W-CVD to come next.
	CVD8999	special | particles ctrl meas	SURF3orSURF5	'0008	
	CVD8899	special | thickness ctrl meas	EUP2or3or4or5or6or7	'0009	
FRONT_W_ABSORB_FSM	MTL6873	100 SE 250 TiN	MDEND2-IPP-2C	'0010	
	MTL2012	12K tungsten, 475C, lower stress MEMS	MDWCNT-D	'0011	
	MTL8499	special | FSM1 measurement	FSM1orFLEX1	'0012	
W_TOUCH_POL	CMP1959	special | WCMP w/W2000	CMP3orCMP7	'0013	Minimal polish needed to make surface look smooth, metallic, mirror-like, but would like to retain as much thickness as we can.
	CMP1840	W scrub	SCB3orSCB4	'0014	
	CMP1873	CMP decontamination, 100:1 HF, 15 secs	WB26-TANK1	'0015	
	CMP0900	spin rinse dry	SRD23	'0016	
	CMP8499	special | FSM1 measurement	FSM1orFLEX1	'0017	
CVD_GRAT_CAP	CVD2999	special	PSKA-TEOSorPSKB-PSGPENorPSKC-SPUTR	'0018	Need 500 nm PETEOS deposition.
	CVD8999	special | particles ctrl meas	SURF3orSURF5	'0019	
	CVD8899	special | thickness ctrl meas	EUP2or3or4or5or6or7	'0020	
ASI_HM_DEP	CVD2999	special	PSKA-TEOSorPSKB-PSGPENorPSKC-SPUTR	'0021	Need 200 nm a-Si deposition.
	CVD8999	special | particles ctrl meas	SURF3orSURF5	'0022	
	CVD8899	special | thickness ctrl meas	EUP2or3or4or5or6or7	'0023	
NONPROD_TRG_THIN_NIT_UTHO	LIT5170	U210/AR2 0.45uM Alt Bake	FSI1orFSI2orFSI5	'0024	LIT5170 4500A UV210 130PEB Shoot at NA = 0.8 on ASML5, try for 0.15 um line LCF, i.e. LCF "A".
	LIT5364	4X DUV exposure: non prod	ASML1orASML5	'0025	
	LIT8195	special | litho CDs no EDC	SEM6orSEM7	'0026	
	LIT8714	CMOS7 detailed PR inspection	OPTI1orOPTI2	'0027	
SI_RIE	DRY4099	special | silicon etch	EPCNT1-CorEPCNT1-D	'0028	Dry etch 200 nm a-Si.
OXETCH1	DRY4699	special | oxide etch	EMEMCNT-BorEOCNT-AorC	'0029	Dry etch 500 nm PETEOS.
HAR_W_ETCH	DRY4599	special | W etch	EPCNT1-D	'0030	Develop high aspect ratio dry etch of 1200 nm tungsten.
	DRY4224	ASP 250C	EMCNT1-DorEMCNT2-DorEOCNT-D	'0031	
SI_RIE_ISO_ASP	DRY4099	special | silicon etch	EPCNT1-CorEPCNT1-D	'0032	Isotropic etch of a-Si layer residuals, if any.
	DRY4224	ASP 250C	EMCNT1-DorEMCNT2-DorEOCNT-D	'0033	
EndLot	COM9930	Box Transfer	zCOMArea	'0034	
	COM0050	take ownership	zCOMArea	'0035	
	COM0010	End Lot	zCOMArea	'0036	

Figure 10. Lot process plan ABSORB_W_ETCH_FOX utilized for RJ137001B/A lots. Red text indicates non-standard steps requiring special instructions and/or development. Green steps prior to dry etches have been completed successfully on lead RJ137001B wafers.

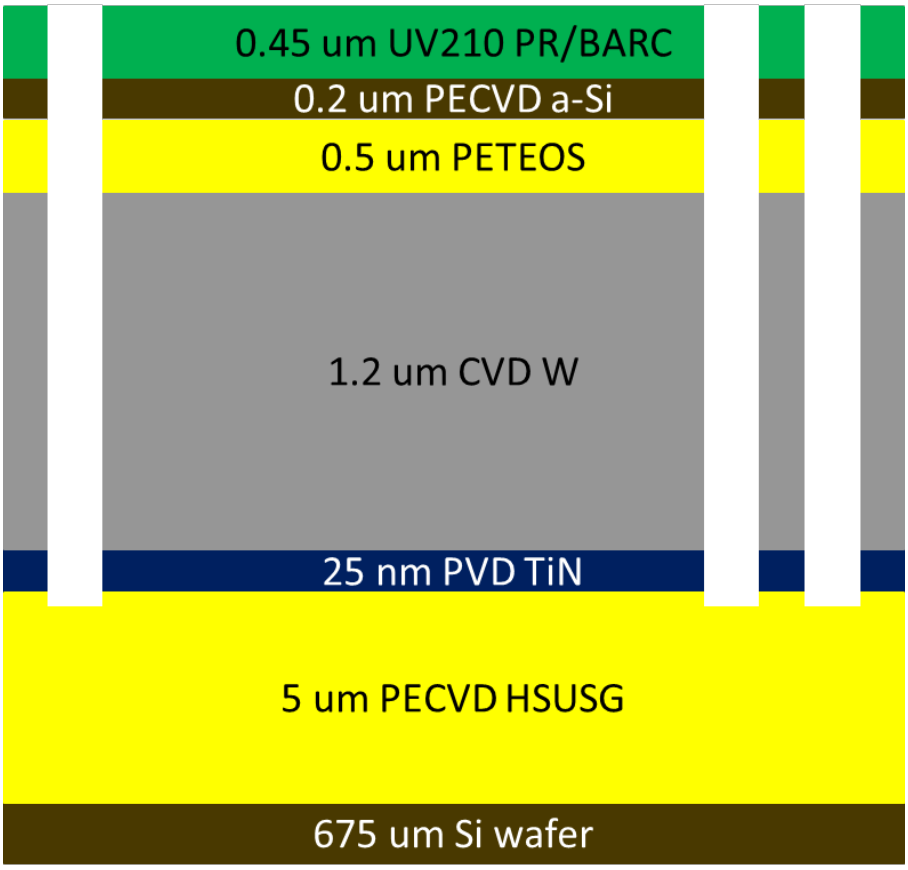

Figure 11. Schematic of final intended stack following DRY4599 Tungsten etch step 30 of process flow.

At this point in the fabrication, the wafer film stack is complete and ready for non-standard ASML 248 nm scanner lithography, in this case employing NA = 0.8 numerical aperture, a fairly thin 0.45 µm UV210 photoresist, on a standard 30 nm base anti-reflective coating (BARC), and an alternate post-exposure bake, all for enhanced resolution for sub-wavelength lines and spaces. A photomask was designed (layout shown in Figure 12) with nine different geometries of the meta-structures (see table in Figure 12). Using a 150 nm line, 150 nm space 1d grating linewidth control feature for targeting, an initial RJ137001B lead lot has completed lithography, and will next receive the a-Si hard mask etch, once a final inspection for some focus spots has been completed. Figure 13 shows how the nine different device designs fared patterning-wise. The a-Si etch including BARC open step is reasonably standard, but getting good performance for a vertical etch on a PETEOS at what is a reasonably high aspect ratio is also critical here, without exceeding the existing mask budget.

Presuming good hard mask patterning, the Tungsten etch is the major remaining challenge. We can leverage some etch recipes developed for high aspect ratio silicon etching as a novel approach to this direct patterning challenge, though Tungsten cannot be expected to etch with equivalent rate, selectivity, profile, or sidewall roughness. The wafers made so far will be an excellent test bed for etch development and evaluating the manufacturability of the current approach, and ultimately for optical performance and thermal endurance testing. If we can validate the etches and hard mask scheme, it may be possible to use the same base film stack to coat with PR and send to the µFab for e-beam patterning tests to achieve much higher effective feature resolutions in the future.

Metastructure Array Geometries

Geometry ID	w (nm)	d (nm)
1	150	300
2	175	350
3	200	800
4	250	500
5	300	600
6	350	500
7	400	800
8	500	900
9	200	3000

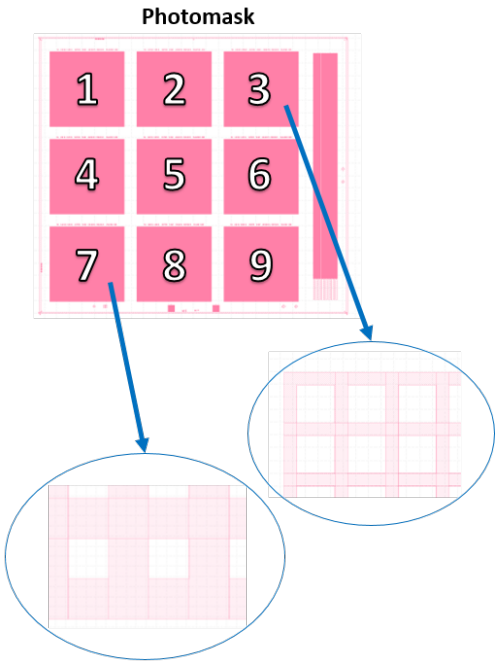

Figure 12. A table of metamaterial structure geometries (left) and corresponding photomask that contain the 2D array of those geometries (right).

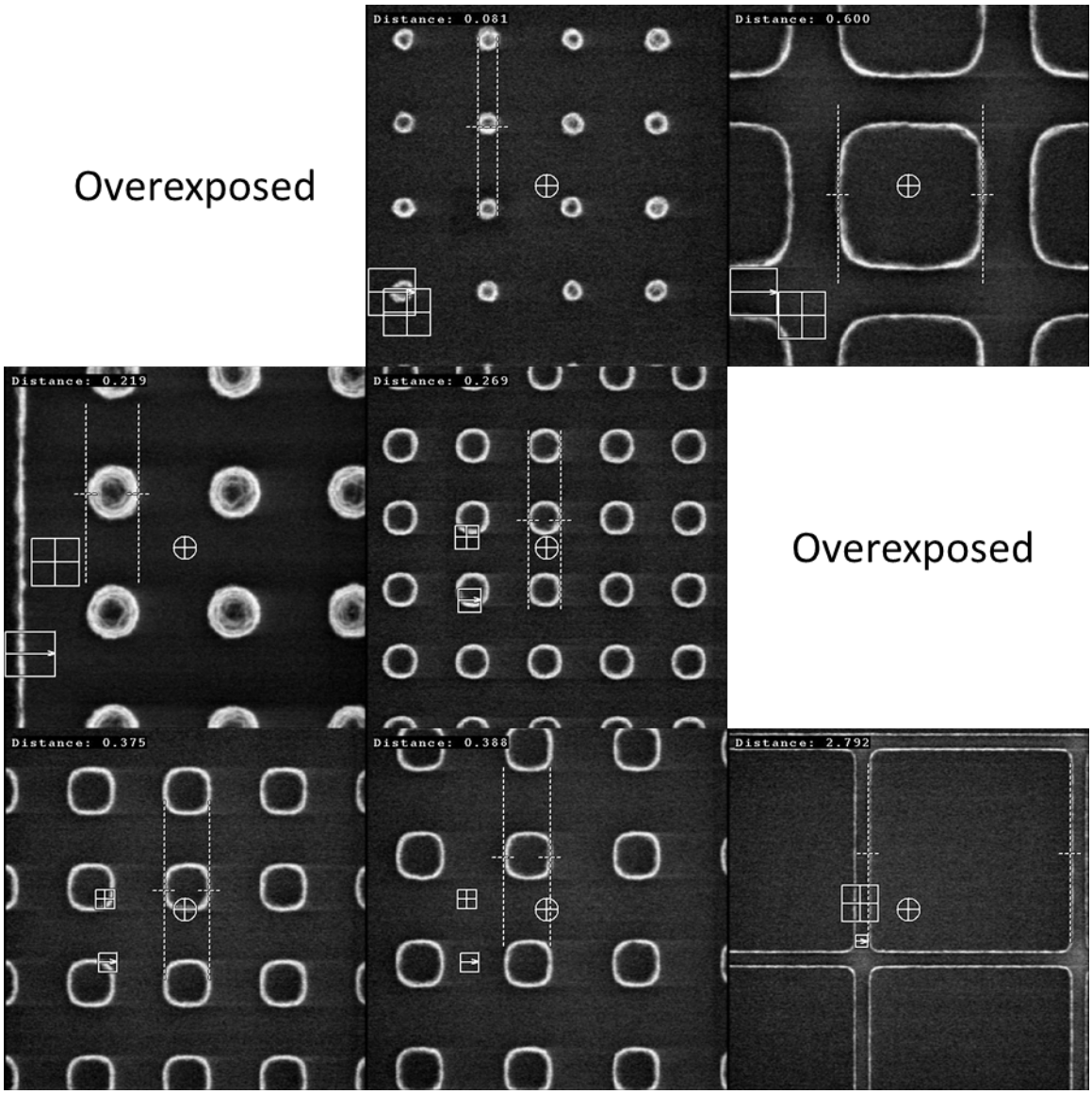

Figure 13. Plan view images (3x3) of ASML patterning on RJ137001B of nine intended 2D grating devices from Nanosem CD SEM tool – corresponds to the mask layout shown in Figure 12. Measurements shown are all in microns.

Devices 1 and 6 (in Figure 13), with 150 nm drawn posts, were overexposed leaving nothing, although 1D grating 150 nm line, 150 nm space structures patterned successfully. Grating 2 (top, middle) shows 81 nm diameter pillars remaining from similar overexposure effects on a drawn 175 nm square post, with a 175 nm space. We believe that the small pillars might be resolved with tailored exposure future targeting adjustments, but almost certainly with failure to open smaller spaces in other grating structures, in particular Grating 9 (bottom, right).

Etch profile, rate, and selectivity to mask will be assessed via cross-section SEM imaging of various dimension test structures during development. Any remaining organic PR/BARC mask or sidewall polymer can then be reactively removed by oxygen atoms from a downstream plasma

ashing process, and remnant a-Si hard mask by isotropic, fluorine-based Si dry etch. Residual PETEOS hard mask will be best dealt with by timed dielectric dry etching.

4. CONCLUSIONS

There is interest in concentrating solar power to go to higher temperatures (≥700°C) to increase the power cycle efficiencies to ≥50% (e.g., with sCO_2 power cycles). However, with current receiver coatings such as Pyromark, the radiative losses increase dramatically with temperature thus reducing the receiver thermal efficiencies. The coatings also degrade under continuous concentrated solar exposures necessitating re-application of the coating every few years, which adds to the O&M costs of the CSP plant. To overcome these challenges, we proposed to develop metamaterials using refractory high-temperature metals to increase the receiver thermal efficiencies at high temperatures. Metamaterials can be designed for high absorptivity in the visible spectrum while making it reflective in the near IR. The flexibility of the plasmonic Brewster angle concepts makes this an ideal solution for developing high temperature receivers that perform with high efficiency.

In this report, we have discussed our progress in analyzing tapered and untapered metamaterial structures made of Tungsten (W), highly doped silicon (P-plus Si) and silicon (Si) for broadband absorption. Based on the concept of plasmonic Brewster angle, periodic slit arrays have been shown to achieve non-resonant, broadband absorption with a choice of broad angle and direction-selective absorption. The design parameter space has been exhaustively explored to tailor the design parameters in order to manipulate the absorption in the structure for a wide range of incident angles and frequencies. We have shown that, by manipulating the geometrical parameters and the materials employed it is possible to control the lower cut-off wavelengths, and create a sharp transition at the desired wavelength between a highly absorptive angle-independent broadband regime and a low-absorptive regime. These properties are ideal for high-temperature CSP receivers. Tungsten (W) appears to be an ideal material for high temperature applications, and has potential disruptive applications for energy harvesting based on these concepts. Other high temperature refractory metals will be explored in future projects.

We have attempted to fabricate some of the geometries designed for high absorptivity in the visible solar spectrum and low absorptivity in beyond a cut-off in the near IR. The fabrication steps were not completed during the project period, although fabrication and optical testing activities were added later in the project with a plus-up support from the LDRD office. In the future small samples of the metamaterials will be fabricated and characterized. Diffuse spectral reflectance will be measured at room temperature using Fourier Transform (FTIR) and ultraviolet/visible/near-infrared (UV/V/NIR) spectrophotometers. From the reflectance measurements, the spectral absorptance and emittance can be calculated. The emittance will also be measured by heating the samples to the expected receiver operating temperature and observing the thermal emission spectrum. The thermal stability of the structure will be investigated using both an isothermal aging protocol and a cycled solar irradiance aging protocol. For the isothermal aging, samples will be placed in a box furnace, heated to the target temperature (600, 700, or 800°C), and held isothermally for a period of time before being cooled down. For the cycled irradiance aging, samples will be exposed to square-shaped periodic solar irradiance cycles over an extended period

of time. After each aging process, we will again measure the optical properties and inspect the surface for defects using a scanning electron microscope (SEM). These tests were not performed during this performance period, but are left as future work.

There are some technical challenges we have considered. Many of the refractory metals possess attractive thermal and plasmonic properties, but are known to oxidize at high temperature in air. The formation of a thermal oxide on metamaterial structures is suspected as the cause for higher-than-expected thermal emittance in the NIR [9]. These impacts will be investigated in the future. Other materials that we will investigate, such as silicon carbide, have the necessary thermal stability but may not support the necessary surface plasmon waves nor be compatible with microfabrication techniques. Another challenge is the large-scale fabrication of the metamaterial structures. We are considering processes such as nano-printing and roll-printing, which have been maturing over the past few years.

REFERENCES

[1] REN21 (2015), Renewables 2015: Global Status Report.

[2] DOE (2012), SunShot Vision Study.

[3] Kennedy, C.E., *Review of Mid- to High-Temperature Solar Selective Absorber Materials*, in *Other Information: PBD: 1 Jul 2002*2002, National Renewable Energy Laboratory: Golden, CO.

[4] Ambrosini, A., et al. *Improved high temperature solar absorbers for use in concentrating solar power central receiver applications*. in *ASME 2011 5th International Conference on Energy Sustainability*. 2011. American Society of Mechanical Engineers.

[5] Ambrosini, A., et al., *High temperature solar selective coatings for solar power central receivers*, 2013, Sandia National Laboratories.

[6] Hall, A., A. Ambrosini, and C.K. Ho, *Solar selective coatings for concentrating solar power central receivers.* Advanced Materials & Processes, 2012. **170**(1): p. 28-32.

[7] Pendry, J.B. *Metamaterials and the Control of Electromagnetic Fields*. in *Conference on Coherence and Quantum Optics*. 2007. Optical Society of America.

[8] Schuller, J.A., et al., *Plasmonics for extreme light concentration and manipulation (vol 9, pg 193, 2010).* Nature Materials, 2010. **9**(4).

[9] Wang, H., et al., *Highly efficient selective metamaterial absorber for high-temperature solar thermal energy harvesting.* Solar Energy Materials and Solar Cells, 2015. **137**(0): p. 235-242.

[10] Wang, H. and L. Wang, *Perfect selective metamaterial solar absorbers.* Opt Express, 2013. 21 Suppl 6: p. A1078-93.

[11] Argyropoulos, C., et al., *Broadband absorbers and selective emitters based on plasmonic Brewster metasurfaces.* Physical Review B, 2013. **87**(20).

[12] A. Alù., et al. (2011). Plasmonic Brewster Angle: Broadband Extraordinary Transmission through Optical Gratings, Phys. Rev. Lett. 106, 123902 (2011).

[13] A. Alù, and N. Engheta, J. Opt. Soc. Am. B 23, 571 (2006).

[14] A. Alù, M.G. Silveirinha, and N. Engheta, Phys. Rev. E78, 016604 (2008); A. Alu` and N. Engheta, Phys. Rev. Lett. 103, 043902 (2009).

[15] C. Argyropoulos, and A. Alù et al. (2012). Matching and funneling light at the plasmonic Brewster angle. PHYSICAL REVIEW B 85, 024304 (2012).

[16] CST Design Studio 2015, http://www.cst.com.

[17] E. D. Palik, Handbook of Optical Constants of Solids (Academic Press, New York, 1985).

[18] K. N. Rozanov, "Ultimate thickness to bandwidth ratio of radar absorbers," IEEE Trans. Antennas Propagat. 48, 1230-1234 (2000).

DISTRIBUTION

Sandia:

1	MS0899	Technical Library	9536 (electronic copy)
1	MS0359	D. Chavez, LDRD Office	1911 (electronic copy)


Sandia National Laboratories